The Astrophysical Journal, 891:46 (14pp), 2020 March 1 https://doi.org/10.3847/1538-4357/ab723d

Deciphering the 3D Orion Nebula-I: Expanding Shells in the Huygens Region

C. R. O'Dell[1], N. P. Abel[2], and G. J. Ferland[3]
[1] Department of Physics and Astronomy, Vanderbilt University, Nashville, TN 37235-1807, USA
[2] MCGP Department, University of Cincinnati, Clermont College, Batavia, OH, 45103, USA
[3] Department of Physics and Astronomy, University Of Kentucky, Lexington, KY 40506, USA
Received 2019 December 10; revised 2020 January 31; accepted 2020 February 1; published 2020 March 3

Abstract

Based on imaging and spectroscopic data, we develop a 3D model for the Huygens Region of the Orion Nebula. θ^1 Ori C, the hottest star in the Trapezium, is surrounded by a wind-blown Central Bubble that opens SW into the Extended Orion Nebula. Outside of this feature lies a layer of ionized gas at about 0.4 pc from θ^1 Ori C. Both of these features are moving rapidly away from θ^1 Ori C with an expansion age for the Central Bubble of only 15,000 yr.

Unified Astronomy Thesaurus concepts: H II regions (694)

1. Introduction

H II regions are important in understanding measurable information such as the abundance of elements throughout our Galaxy. This extends to the study of more distant galaxies, because the copious Far Ultraviolet radiation of their hot ionizing stars are efficiently concentrated, through the process of photoionization, into easily observed emission lines. What occurs in H II regions also affects the process of star formation in massive galactic clusters and may stimulate waves of star formation through their compression of surrounding interstellar gas and dust. The Orion Nebula together with its associated Orion Nebula Cluster is the closest region of star formation that involves massive stars and presents the best opportunity to understand the processes that occur. These may then safely be assumed to operate in more distant and difficult-to-observe H II regions.

The major goal of the present paper is to use optical data to understand the 3D structure of the central portion of the Orion Nebula. This will include determining the structure from the Main Ionization Front (MIF) on the surface of the host Orion Molecular Cloud (OMC) through the outermost shells of atomic gas that cover this region. In a subsequent paper (Paper II; C. R. O'Dell et al. 2020, in preparation), we will address how the imbedded Orion-S Cloud affects the structure in the southwest portion of the nebula.

1.1. Background

There is a rich literature on the Orion Nebula (Ferland 2001; O'Dell 2001; Muench et al. 2008; O'Dell et al. 2008; Goicoechea et al. 2015; Kong et al. 2018; Pabst et al. 2019). Most of the emission occurs in an ionized blister of gas on the concave Photon Dominated Region (PDR) within the facing surface of the host OMC. As the gas flows toward the observer from the PDR it is ionized and accelerated. In the vicinity of the strong stellar wind from θ^1 Ori C, one expects a hot bubble to be created, which was identified and characterized from *Hubble Space Telescope* (*HST*) images (O'Dell et al. 2009). Proceeding further toward the observer, one encounters a layer of ionized gas called Component I in Abel et al. (2019), and we designate as the Nearer Ionized Layer (NIL), and then two layers of atomic gas (together called the Veil; van der Werf & Goss 1989, 1990; Abel et al. 2004, 2006, 2016; van der Werf et al. 2013).

The brightest part of the nebula is called the Huygens Region (after the first astronomer to publish a drawing of the Orion Nebula). With a characteristic angular size of 4′ (0.4 pc),[4] it occupies the northeast corner of a much larger structure (34.′7 (3.9 pc) north–south and 30.′1 (3.3 pc) east–west). The portions outside of the Huygens Region are called the Extended Orion Nebula (EON; Güdel et al. 2008). The inner atomic component of the Veil appears to be a shell of material that envelopes the entire nebula (both the Huygens Region and the EON) Pabst et al. (2019) with a line-of-sight (LOS) separation from θ^1 Ori C of about 2.0 pc (Abel et al. 2019).

The dominant ionizing star in the Huygens Region is θ^1 Ori C, lying about 0.15 ± 0.05 pc (O'Dell et al. 2017) in front of the MIF, with the next most important star being θ^2 Ori A (O'Dell et al. 2017) that lies 135″ to the southeast. Along the LOS toward the MIF and its underlying PDR, the Spectral Energy Distribution of θ^1 Ori C is modified as it passes through the ambient gas, first in a He^++H^+ region that hosts the [O III] (500.7 nm) emission and then through a thin He^o+H^+ layer that produces the [N II] (658.3 nm) emission close to the MIF. An underlying consideration in the analysis of the MIF emission is that the expected thickness of the He^++H^+ zone that produces the $V_{mif,[N\,II]}$ emission should be thinner than the He^o+H^+ zone that produces the $V_{mif,[O\,III]}$ emission. Baldwin et al. (1991) estimated that the H^+ emitting zone (which is where most of the [O III] emission occurs) is about 0.09 pc, corresponding to 48″ at our adopted distance. O'Dell (2018) cites model predictions for e^{-1} thicknesses of 0.0012 pc (0.″6) for [N II] and 0.026 pc (14″) for [O III]. In the same paper, a profile of the Bright Bar (that must be tilted close to the LOS) gives thicknesses of 2.″7 (0.005 pc) and 8″ (0.015 pc) for [N II] and [O III], respectively, with the former value probably being an upper limit since the Bright Bar was not resolved below that size.

The 3D structure of the Huygens Region has been the subject of multiple studies (Wen & O'Dell 1993; O'Dell et al. 2009, 2017). These can be summarized as a concave structure marked by two significant features. To the southeast of θ^1 Ori C is a linear escarpment (seen as a bright, low-ionization, linear feature called the Bright Bar crossing most of the Huygens Region) and

[4] We adopt the distance of 383 ± 3 pc derived by Kounkel et al. (2016), which is in agreement with more recent results using *Gaia* DR2 (Großschedl et al. 2019). This distance gives a scale of 1.86×10^{-3} pc/″.

a bump in the surface to the southwest of θ^1 Ori C commonly associated with the Orion-S Cloud.

There are three regions of recent star formation within the Huygens Region. The only one visible in the optical is the eponymous Orion Nebula Cluster. 60″ at position angle 336° from θ^1 Ori C is the highly imbedded BN–KL young star region visible only in infrared and radio wavelengths except for shocks at the tips of fingers radially distributed about a common center. The motion of the optical shocks give an upper limit for their age of 1000 yr (Doi et al. 2004), and their origin is most likely a dynamical event that arose some 500 yr ago (Gómez et al. 2005; Rodríguez et al. 2005). Knowledge of the proper motion, radial velocity, and direction of the origin place it 0.2 pc behind the local MIF (Doi et al. 2004). The third star formation region lies to the southwest of the Trapezium stars and is the subject of Paper II.

A less obvious feature that is important to this study is an arcuate structure surrounding θ^1 Ori C. Its reality was established in O'Dell et al. (2009) where it was shown to be composed of three arcs of [N II] and [O III] emission (designated there as the [O III] Shell, the Big Arc east, and Big Arc South and in this study collectively as the High Ionization Arc). This feature is approximately circular near the Trapezium stars but opens to the southwest, in the direction of the Orion-S Cloud. García-Díaz et al. (2008) establish that it has a characteristic radial velocity of 10 km s^{-1} and extends as far east as the R.A. of θ^2 Ori A.

1.2. Nomenclature

A note on the nomenclature of this paper is in order. Large Samples are areas of 10″ × 10″ within which spectra from a spatially resolved atlas of spectra of certain emission lines have been averaged. Regions are groupings of Large Samples. The Huygens Region is the brightest part of the Orion Nebula and is in the northeast corner of the EON.

Velocities are always given in km s^{-1} in the Heliocentric reference frame and can be converted to the LSR velocity by subtracting 18.1 km s^{-1}.

Directions such as northeast and southwest are often expressed in short form as NE and SW.

1.3. Outline of This Paper

After presenting the background to the subject of this paper (Section 1.1) and the outline presented in this section, we present the observational data that we use, their sources, and how we extracted the information used in this paper (Section 2). Testing and determination of the photoevaporation model is presented in Section 3. The characteristics and origin of the weaker velocity components are the subject of Section 4. The regions of locally high extinction are evaluated in Section 5. All of the observations are used to develop a 3D model of the nebula in an LOS toward the Trapezium, including a calculation of photo-ionization models for the NIL are given in Section 6. The properties of the Central Bubble, the colliding layers, a putative relation between the V_{low} and V_{mif} components, and a recently presented alternative 3D model are discussed in Section 7. Our conclusions are summarized in Section 8. In the A, we illustrate how the observed velocity values are divided into components, how the visibility of weak components on the shoulders of strong components depends on the Full Width at Half Maximum (FWHM) of the strong component, how the magnetic field of the PDR varies in the vicinity of the Orion-S Cloud, and a revised table of velocities in the central Huygens Region is given.

2. Observations

As in our earlier studies (O'Dell 2018; Abel et al. 2019), we have drawn on the high spectral resolution Spectroscopic Atlas of Orion Spectra (henceforth "the Atlas"; García-Díaz et al. 2008). The Atlas was compiled from a series of north–south spectra at intervals of 2″ and that have a velocity resolution of 10 km s^{-1}. The resolution along each slit was seeing limited at about 2″.

We employed emission-line images made with the *HST* (O'Dell & Wong 1996; O'Dell et al. 2009) that isolate diagnostically useful emission lines covering the Huygens Region.

We use the results from Goicoechea et al. (2015), which included all of the Huygens Region but did not go extensively into the EON. Goicoechea et al. (2015) reported on Herschel satellite spectra of the 158 μ [C II] line at 0.4 km s^{-1} and 11.″4 resolution. The study also presented H41α observations with the IRAM-30 m telescope. These had 0.65 km s^{-1} and 27″ resolution. Their discussion also used CO 2–1 observations by Berné et al. (2014) at 0.4 km s^{-1} and 11″ resolution.

2.1. Large Samples of Spectra

O'Dell (2018) grouped spectra from the Atlas into averages over areas of 10″ × 10″ designated here as Large Samples. The higher signal-to-noise ratio (S/N) of these Large Samples were at the expense of spatial resolution. O'Dell (2018) evaluated 65 Large Samples, collectively calling them the NE Region. Abel et al. (2019) used 32 of these Large Samples to define an area also called the NE Region, a name we use in the present paper because we build upon the Abel et al. (2019) paper. The NE Region was used in Abel et al. (2019) to study a large column toward θ^1 Ori C that was expected to be free of the effects of the Orion-S Cloud. In order to characterize conditions in a broader area, we have employed a grouping of 32 samples called the SW Region, and another of 27 Large Samples designated as the SE Region. In addition, samples composed of multiple Large Samples used to study regions of high extinction in Abel et al. (2019) were used. All of these large regions are shown in Figure 1.

2.2. Characteristic Velocity Systems

The use of the IRAF[5] task "splot" has shown that deconvolution of the Atlas spectra (O'Dell 2018) and earlier higher-velocity resolution spectra (Castañeda 1988; O'Dell & Wen 1992; Wen & O'Dell 1993; Doi et al. 2004) reveal common emission-line features in multiple areas. For strong lines, the accuracy of the derived velocity is about 1 km s^{-1}. In this paper, we often give velocities to an accuracy of 0.1 km s^{-1} (most meaningful when averaging large numbers of velocities) but round-off to the nearest integer when the uncertainty is large.

We have used the distinguishing properties adopted in Abel et al. (2019; only slightly different from those used by O'Dell 2018) for different velocity systems. V_{blue} components

[5] IRAF is distributed by the National Optical Astronomy Observatories, which is operated by the Association of Universities for Research in Astronomy, Inc. under cooperative agreement with the National Science foundation.

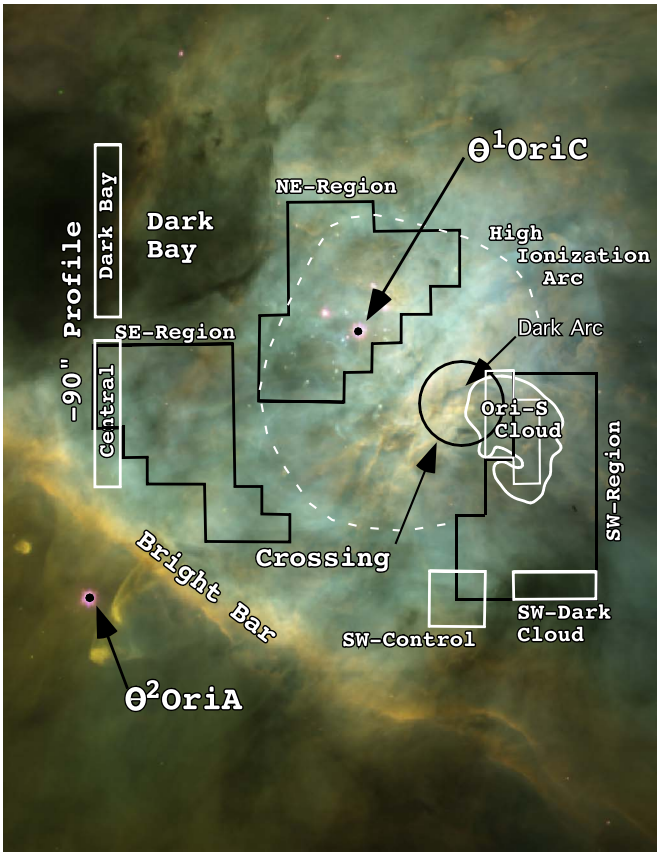

Figure 1. This 233″ × 302″ (0.43 × 0.56 pc) image centered 36″ at PA = 166° from θ^1 Ori C is a portion of the Huygens Region (O'Dell & Wong 1996) and is color coded as follows: blue [O III], green Hα, and red [N II] emission. North is up, west is to the right, and east is to the left. The white solid curved line indicates the edge of the Orion-S Cloud as seen in H I 21 cm absorption (van der Werf et al. 2013). The dashed white line indicates the position of the High Ionization Arc. The NE Region studied in Abel et al. (2019) plus the SW Region and SE Regions added in the current study are shown with black boundaries. The white boxes indicate samples taken to study high-extinction regions. The black circle labeled "Crossing" indicates the region thought to be the most important area for studying the optical features at the NE boundary of the Orion-S Cloud. It is most completely designated as the Ori-S or Orion-S Crossing but frequently called here the "Crossing."

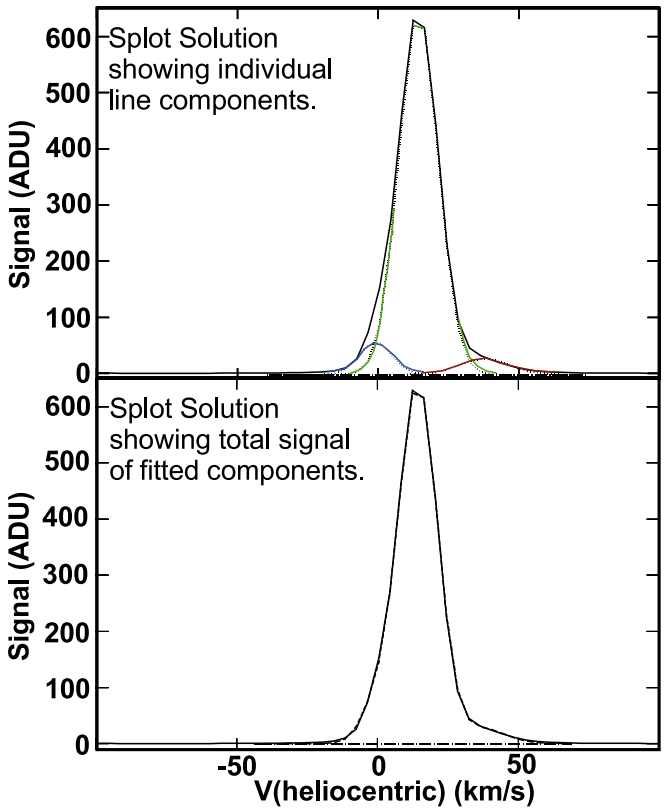

Figure 2. The results of using package "splot" to fit the observed line profile of the [O III] 500.7 nm line is shown. The lower panel shows that the fitted accumulative components are indistinguishable from the observed profile. The upper panel shows the individual components whose sum produces the fit in the lower panel.

$\leqslant -10$ km s^{-1} are assumed to belong to outflows from young stars that create shocks in the ambient nebular gas (O'Dell et al. 2008), rather than the large-scale pattern of the V_{low} spectra. They are not used in our analysis.

In Appendix A, we present a critical analysis of the accuracy of measuring a weak line on the short wavelength shoulder of a strong emission line. There, we see that the accuracy is largely determined by the FWHM of the strongest (V_{mif}) component.

2.2.1. Deconvolution of Large Samples

An illustrative sample of the deconvolution of a Large Sample is shown in Figure 2. In this case, the velocity separations and relative strengths are: MIF 0 km s^{-1}, 1.00; $V_{low,[O\ III]}$ 15.4 km s^{-1}, 0.07; $V_{red,[O\ III]}$ +23.3 km s^{-1}, 0.05. The accuracy of a very weak component lying on the shoulder of the strong V_{mif} component is discussed in Appendix A. The results of the deconvolution of the NE and SW Regions have been published in Abel et al. (2019), and in Figure 3, we show a histogram of velocity components in the SE Region, together with their average velocities. The peak in occurrence in $V_{[O\ III]}$ at 10 km s^{-1} is due to the High Ionization Arc, as shown in Figures 2 and 15 of Doi et al. (2004), where it should be noted that they express relative velocities with respect to 18 km s^{-1}. No $V_{new,[N\ II]}$ components are seen in the lower panel, while the upper panel shows the difficulty in distinguishing between $V_{mif,[O\ III]}$ and $V_{new,[O\ III]}$ components. The relative strength of components helps to distinguish these velocity-ambiguous components. The results for the deconvolution of the Regions are given in Table 1.

3. Testing the Photoevaporation Model

The basic model of the Huygens Region as a thin ionized layer on the surface of the host OMC was recognized from the expectation that a photoevaporating cloud would accelerate as it left the PDR with observations that agreed with the theoretical expectation. The original papers independently proposing this model (Zuckerman 1973; Balick et al. 1974) drew on the limited velocity information then available, recognizing that the higher-ionization material (further from the PDR and closer to θ^1 Ori C) had a more negative radial velocity than the lower ionization material. This model has been refined by recognition of the concave structure of the MIF (Wen & O'Dell 1995) and recognition that the velocity variations across the nebula but within the same ion are due to local smaller scale variations in the tilt of the PDR (O'Dell 2018).

The V_{mif} values in Table 1 are all lower than the reference V_{PDR} velocity of 27.3 ± 0.3 km s^{-1} that we have adopted (O'Dell 2018). $V_{mif,[N\ II]}$ values are always higher than $V_{mif,[O\ III]}$, which is consistent with the He^o+H^+ layer (producing $V_{mif,[N\ II]}$

Table 1
Results for Regions

	NE Region	NE Region	SE Region	SE Region	SW Region	SW Region
Component	[N II]	[O III]	[N II]	[O III]	[N II]	[O III]
V_{scat}	40.3 ± 3.4	37.9 ± 3.1	39.4 ± 3.1	41.0 ± 5.2	38.8 ± 3.2	37.6 ± 2.6
V_{new}	36.5 ± 1.8	27.4 ± 5.4	···	26.5 ± 1.7	33.3 ± 2.2	26.9 ± 7.6
V_{mif}	22.4 ± 2.2	18.0 ± 2.8	23.8 ± 2.3	19.0 ± 2.9	18.0 ± 1.8	10.8 ± 2.8
V_{low}	5.6 ± 3.7	7.8 ± 2.1	5.5 ± 2.7	5.5 ± 3.0	2.8 ± 1.9	0.7 ± 3.3
V_{blue}	−6.1 ± 2.8	0.6 ± 3.8	−12.3 ± 1.5[a]	−4.8[b]	−4.2 ± 3.1	−0.8 ± 4.7
S_{scat}/S_{mif}	0.06 ± 0.03	0.06 ± 0.03	0.060 ± 0.026	0.048 ± 0.034	0.06 ± 0.03	0.07 ± 0.03
S_{low}/S_{mif}	0.10 ± 0.03	0.13 ± 0.12	0.25 ± 0.11	0.13 ± 0.08–0.95 ± 0.26[c]	0.10 ± 0.03	0.09 ± 0.02–0.65 ± 0.19[c]

Notes.
[a] Two Large Samples only.
[b] One Large Sample only.
[c] Values cluster around these two values.

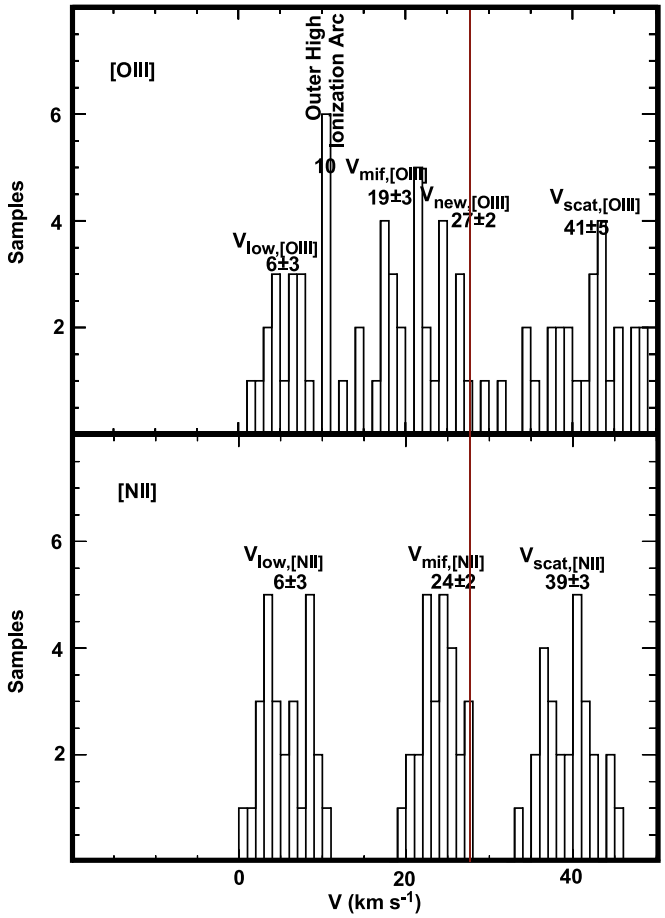

Figure 3. These histograms for the SE Region show the frequency of line components in both [N II] and [O III] and are discussed in Section 2.2.1. The red line indicates the adopted velocity of the PDR (27.3 km s^{-1}).

emission) not having been accelerated away from the PDR as the He^++H^+ layer that produces the $V_{mif,[O\ III]}$ emission.

The V_{evap} values derived from our assumed V_{PDR} and the V_{mif} NE-Region and SE-Region values of Table 1 are $V_{evap,[N\ II]} = 4 \pm 3$ km s^{-1} and $V_{evap,[O\ III]} = 9 \pm 3$ km s^{-1}. Quite different values are derived from the SW Region ($V_{evap,[N\ II]} = 9 \pm 2$ km s^{-1} and $V_{evap,[O\ III]} = 16 \pm 3$ km s^{-1}). The differences in the derived V_{evap} for the regions could be that the SW Region is more nearly flat-on as viewed by the observer than the other two regions.

The photoevaporation model can also be tested using the results of Goicoechea et al. (2015), who studied 158 μ [C II] emission across the nebula, with particular emphasis on a region centered on θ^1 Ori C, which lies within our NE Region. This radiation arises within the PDR. Immediately behind the PDR lies the CO emitting layer in the background molecular cloud. Their Figure 3 shows that $V_{[C\ II]}$ and V_{CO} are at 28 km s^{-1} (10 km s^{-1} in the LSR velocity system they use). Recombination hydrogen emission H41α is at 16 km s^{-1} (−2 km s^{-1} LSR). Since ionization models show that the hydrogen radiation should arise mostly from the [O III] emitting layer, these data indicate that $V_{evap,H\ II} = 12 \pm 2$ km s^{-1}, greater than $V_{evap,[O\ III]} = 9 \pm 3$ km s^{-1} and 8 ± 3 for the NE and SE Regions, but less than 16 ± 3 for the SW Region.

For the remainder of this paper, we will adopt $V_{evap,[N\ II]} = 7 \pm 4$ km s^{-1} and $V_{evap,[O\ III]} = 12 \pm 4$ km s^{-1}.

4. Origin of the Weaker Velocity Components Seen in the Large Samples

The strongest velocity component (V_{mif}) arises from the MIF lying immediately on the observer's side of the ionization front along the PDR. In this section, we will illustrate the features and the interpretation of the weaker components within the Large Samples. A summary table of all of the velocities except those in the two outermost Veil components is give in Appendix B.

4.1. Origin of the V_{scat} Component

A redshifted component is found in almost all of the Large Samples and the Profile Samples. After the discovery that the nebula's continuum was strong (Greenstein & Henyey 1939a, 1939b), the sources that dominate in the continuum (the Trapezium stars) were established quantitatively by Baldwin et al. (1991). In their comprehensive lower-resolution study, O'Dell & Harris (2010) demonstrated that scattering of nebular emission occurs not only in backscattering by the nearby PDR but also at large distances. However, the redshifted component arises from local backscattering.

The V_{scat} components in the Huygens Region are usually attributed to backscattering by dust in the PDR (Henney 1998; O'Dell 2001, 2018; Abel et al. 2006) lying along the same LOS. Within this model where the emission lines arise from

Table 2
Separation of V_{scat} and V_{mif} Components

Region	$V_{scat,[N\ II]}$–$V_{mif,[N\ II]}$	$V_{scat,[O\ III]}$–$V_{mif,[O\ III]}$
NE Region	18 ± 4	19 ± 4
SE Region	16 ± 3	22 ± 6
SW Region	21 ± 3	27 ± 3
Average	18 ± 4	23 ± 5
Predicted	14 ± 4	24 ± 4

Table 3
S_{scat}/S_{mif}

Region	[N II]	[O III]
NE Region	0.05 ± 0.02	0.06 ± 0.026
SE Region	0.07 ± 0.06	0.04 ± 0.027
SW Region	0.07 ± 0.03	0.08 ± 0.024
Average	0.06 ± 0.04	0.06 ± 0.03

photoevaporation of ionized material away from the ionization front on the PDR, the expected redshift of the backscattered component, relative to the layer producing the V_{mif} emission, is about twice the photoevaporation velocity (Henney 1998). Since $V_{evap,[O\ III]}$ is larger than $V_{evap,[N\ II]}$, the $V_{scat,[O\ III]}$ has a larger redshift, so it is easier to detect. The observed and predicted values of V_{scat}–V_{mif} are given in Table 2. Where we see that $V_{scat,[N\ II]}$–$V_{mif,[N\ II]}$ values are somewhat larger than expected from our adopted values, $V_{evap,[N\ II]}$ and $V_{scat,[O\ III]}$–$V_{mif,[O\ III]}$ are in good agreement.

Table 3 shows that the signal of the V_{scat} component relative to the V_{mif} component varies little between the Regions and is indistinguishably the same in [N II] and [O III].

Models of artificial spectra using the methods of Appendix A and the average FWHM of 16.4 and 13.2 km s^{-1} for [N II] and [O III] showed that the derived properties of the scattering components (V_{scat} and S_{scat}/S_{mif}) agree well with the predictions of models. That is to say, the wide separation of the V_{mif} and V_{scat} components allows for derivations that are unaffected by blending.

4.2. Origin of the V_{low} Component

The component that we call V_{low} is associated with the NIL (called V_{low} and Ionized Component I in O'Dell (2018) and Abel et al. (2019), respectively). Clear evidence for it in the direction of the Trapezium and θ^2 Ori A lie in absorption lines formed there. These are He I at 2.1 ± 0.6 km s^{-1} (O'Dell et al. 1993), P III at 4.9 ± 3.0 km s^{-1} (Abel et al. 2006), S III at 4.5 ± 0.9 km s^{-1} (Abel et al. 2006), Ca II at 7.5 km s^{-1} (O'Dell et al. 1993), and Na I at 6.0 km s^{-1} (O'Dell et al. 1993), for an average of 5.0 ± 2.0 km s^{-1}.

Accurate emission-line velocities for the V_{low} components are more difficult to determine because the lines fall on the shoulders of the much stronger V_{mif} component. In Appendix A, we demonstrate that the limit of detectability of the separation from V_{mif} is determined by the FWHM of the V_{mif} component, which is lying about 0.5 km s^{-1} below the FWHM.

For [N II], the average FWHM is 16.4 ± 0.6 km s^{-1} and the average splitting $V_{mif,[N\ II]}$–$V_{low,[N\ II]}$ in Table 1 is 17 ± 4; thus, the average $V_{low,[N\ II]} = 5 \pm 3$ indicates that the $V_{low,[N\ II]}$ component arises from the same layer as the absorption lines (the NIL).

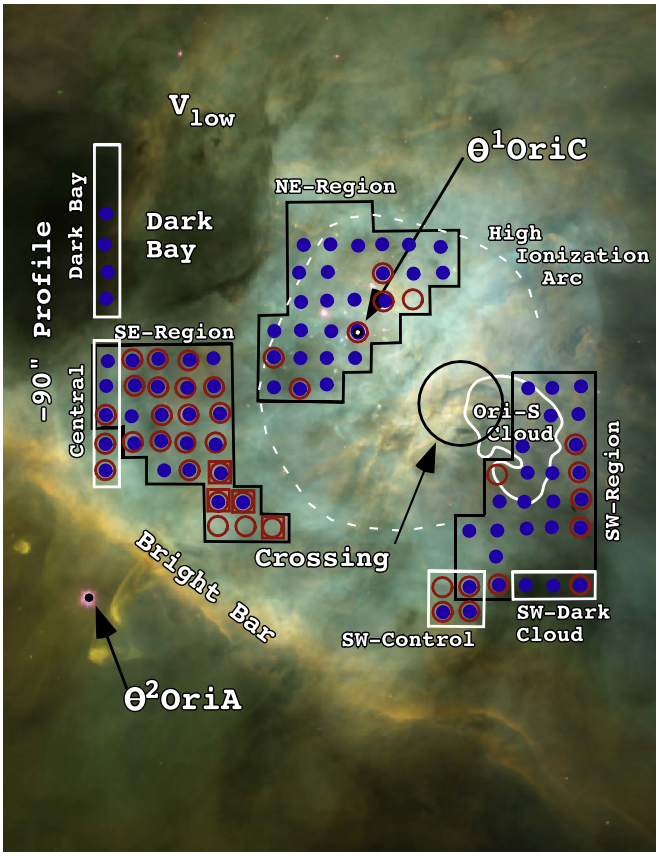

Figure 4. The same as Figure 1, except now we indicate where a V_{low} component is detected (blue filled circles $V_{low,[N\ II]}$, red circles $V_{low,[O\ III]}$). The large open squares indicate where the $S_{low,[O\ III]}/S_{mif,[O\ III]}$ ratio is unusually large.)

The FWHM for the $V_{mif,[O\ III]}$ component is 13.2 ± 0.8 km s^{-1} and the average splitting $V_{mif,[O\ III]}$–$V_{low,[O\ III]} = 11 \pm 3$, indicating that $V_{low,[O\ III]}$ lines are affected by the difficulty of extracting the $V_{low,[O\ III]}$ from the shoulder of the $V_{mif,[O\ III]}$ component. In the much higher-resolution study of [O III] by Castañeda (1988), (FWHM = 10.9 ± 1.9 km s^{-1}) $V_{mif,[O\ III]}$–$V_{low,[O\ III]} = 8.0 \pm 2.6$ km s^{-1}, which is evidence that that the average $V_{low,[O\ III]}$ in the Regions is 8 ± 3 km s^{-1}. Casteñeda employed the KPNO Coude Spectrograph with a resolution $\lambda/\delta\lambda$ of 100,000, giving an instrumental FWHM of 4.0 km s^{-1}, which clearly identified the $V_{mif,[O\ III]}$ FWHM. $V_{low,[O\ III]}$ derived from our value of $V_{mif,[O\ III]}$ and their separation ($V_{low} = 8 \pm 3$ km s^{-1}) is adopted in the remainder of this report.

This value again indicates that the $V_{low,[O\ III]}$ component arises from the same layer as the NIL.

Two additional studies using the same velocity resolution as the Castañeda (1988) study give V_{low} velocities of 3 km s^{-1} for [O II] (Jones 1992) and 10 km s^{-1} for [S III] (Wen & O'Dell 1993), again indicating association with the NIL.

The distribution of where the V_{low} components are seen is shown in Figure 4. The distribution may extend as far as the LOS toward θ^2 Ori A. A high-resolution spectroscopic study of this star (O'Dell et al. 1993) shows two He I* absorption components at −2.9 and 5.2 km s^{-1}, (with uncertainties of about 1 km s^{-1}). The more positive component can be associated with the average of the Regions $V_{low,[O\ III]} = 5 \pm 3$ km s^{-1} and would be evidence that the NIL system extends beyond the inner Huygens Region. Because the 388.9 nm absorption line is

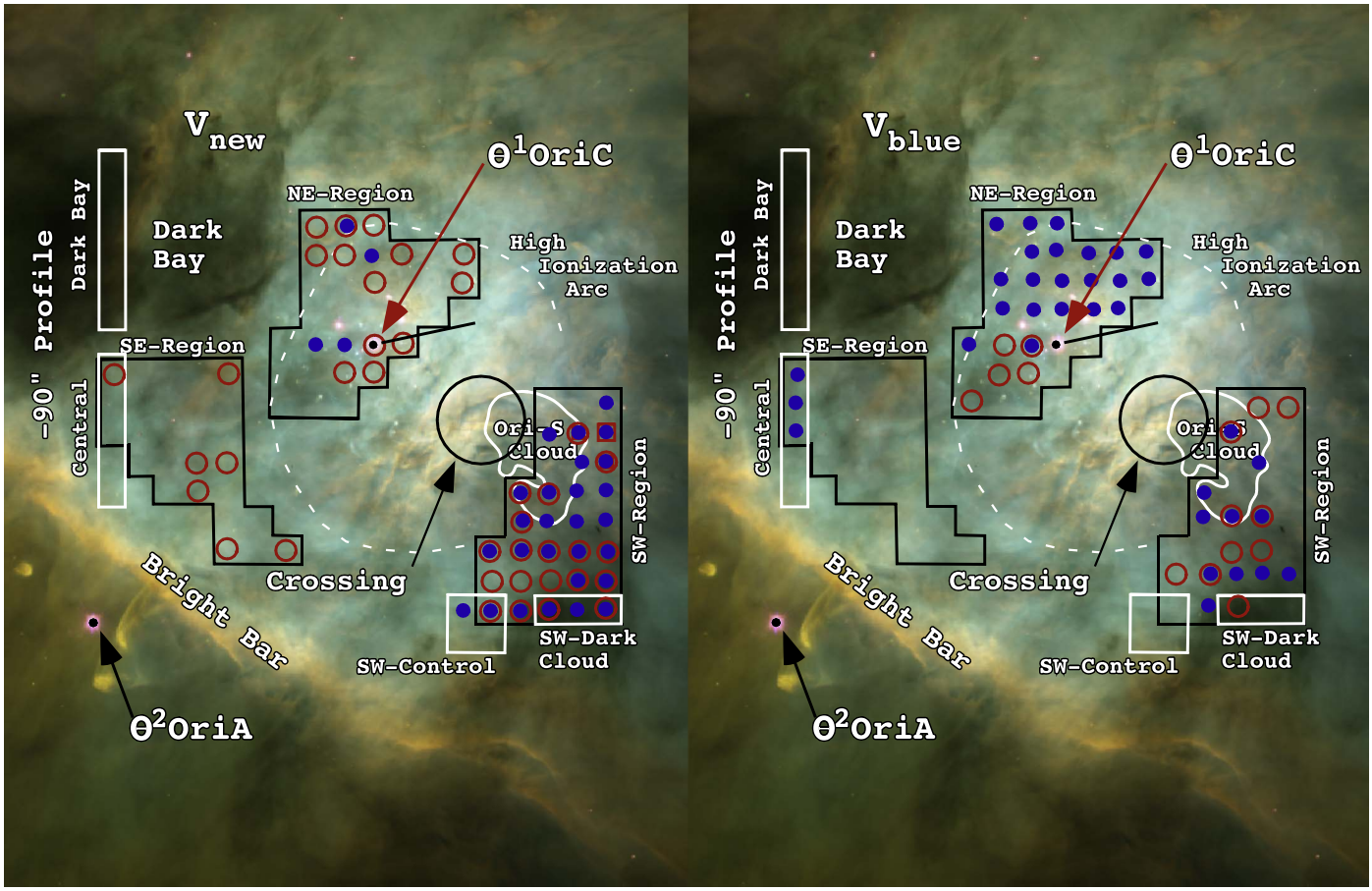

Figure 5. The same as Figure 4, except now we indicate where the V_{new} (left panel) and V_{blue} (right panel) components are detected (blue filled circles indicate [N II] detections and red circles [O III] detections).

formed in gas of the same level of ionization as the $V_{low,[O\ III]}$ emission line, the conclusion that the NIL extends as far as θ^2 Ori A is strengthened by the fact that $V_{low,[O\ III]}$ for the nearby SE Region is 6 ± 3 km s^{-1}.

We can safely conclude that the NIL is real, extends across the inner Huygens Region, has a velocity of about 6 ± 2 km s^{-1}, and is most visible in [N II].

4.3. Origin of the V_{new} and V_{blue} Components

The V_{new} components were originally reported in O'Dell (2018), where they were only detected in [O III], while Abel et al. (2019) found it in [N II]. Our study includes many more large samples than in these previous studies, and the location of the detected V_{new} components are shown in the left-hand panel of Figure 5. The average $V_{new,[N\ II]}$ in the two regions where it is detected is 35 ± 3 km s^{-1}, while the $V_{new,[O\ III]}$ average in the three regions is 27 ± 4.

The V_{blue} components are weaker than the V_{low} components, even after factoring in the classification criteria. Their locations are shown in the right panel of Figure 5. The average $V_{blue,[N\ II]}$ in the two regions where it is frequent is -5 ± 3 km s^{-1}. Similarly, the average $V_{blue,[O\ III]}$ is 0 ± 4 km s^{-1}. Recall that in this tabulation, all of the velocity components $\leqslant -10.0$ km s^{-1} are assumed to belong to outflows from young stars that create shocks in the ambient nebular gas. Including the spectra with $V_{low,[N\ II]} \leqslant 10$ km s^{-1} would decrease the averages by 2.2 km s^{-1}.

Abel et al. (2019) attributes the V_{blue} components to material at the approaching side of an expanding hot shocked bubble surrounding θ^1 Ori C, which they call the Nearer Central Bubble (we will use Central Bubble). Our larger data set comes to the same conclusion if the effects of the Central Bubble extend into the regions immediately outside of the High Ionization Arc. Their attribution of the V_{new} components to shocked gas moving into the high-density MIL is also acceptable, with $V_{new,[N\ II]}$ (35 ± 3 km s^{-1}) moving 15 km s^{-1} faster than the MIF (20 ± 3). Similarly, $V_{new,[O\ III]}$ (27 ± 4 km s^{-1}) moves 11 km s^{-1} relative to the MIF (16 ± 4).

5. High-extinction Regions

The primary source of extinction and reddening in the Huygens Region is the foreground Veil (O'Dell & Yusef-Zadeh 2000). In the latter study, done at higher spatial resolution, it was shown that the greatest extinction occurs in the region known as the Dark Bay, where the logarithmic Hβ extinction coefficient ($c_{H\beta}$) reaches 2.0. This region is crossed by the $-90''$ Profile (O'Dell 2018) where $c_{H\beta}$ is about 1.6 and the results are included in Table 4 under the heading $-90''$ Dark Bay. A second region of high extinction is in the direction of the Orion-S Cloud, where O'Dell & Yusef-Zadeh (2000) found $c_{H\beta}$ about 0.6. This would be a lower limit since the part of the radio continuum used to derive the extinction arises from the side of the Orion-S Cloud that faces the OMC. This region was characterized by six Large Samples as shown in Figure 1. A third region of high extinction is the dark SW Cloud (García-Díaz & Henney 2007), where $c_{H\beta}$ is about 1.0. Three Large Samples were used in O'Dell (2018) to isolate the SW Cloud and another four to isolate a nearby region

Table 4
Comparison of Large Samples Relevant to Discussion of Local Extinction[a]

Sample	$V_{\rm mif,[N\ II]}$	$V_{\rm mif,[O\ III]}$	$V_{\rm low,[N\ II]}$	$V_{\rm low,[O\ III]}$	$S_{\rm mif,[N\ II]}/S_{\rm mif,[O\ III]}$	$S_{\rm low,[N\ II]}/S_{\rm mif,[N\ II]}$	$S_{\rm low,[O\ III]}/S_{\rm mif,[O\ III]}$
−90″ Central Region	23 ± 1	20 ± 2	6 ± 3	6 ± 2	1.7 ± 1.4	0.2 ± 0.1	0.2 ± 0.1
−90″ Dark Bay	28 ± 1	18 ± 0.2	11 ± 3	⋯	3.4 ± 0.6	0.4 ± 0.2	⋯
SE Region	24 ± 2	19 ± 3	6 ± 3	6 ± 3	1.7 ± 0.8	0.25 ± 0.11	0.13 ± 0.08–0.95 ± 0.26[b]
NE Region	22 ± 2	18 ± 3	6 ± 4	8 ± 2	1.5 ± 0.5	0.10 ± 0.03	0.13 ± 0.12
Orion-S Cloud	21 ± 1	11 ± 2	2.6[c]	−1.0[c]	1.7 ± 0.4	0.08[c]	0.07[c]
SW Region	18 ± 2	11 ± 3	3 ± 2	1 ± 3	1.6 ± 0.5	0.10 ± 0.03	0.09 ± 0.02–0.65 ± 0.19[b]
SW Control	17 ± 2	11 ± 3	−2 ± 3	−1 ± 1	1.1 ± 0.2	0.07 ± 0.04	0.07 ± 0.03
SW Cloud	18 ± 2	12 ± 1	−1 ± 3	0 ± 7	1.7 ± 0.1	0.09 ± 0.03	0.06 ± 0.03

Notes.
[a] All velocities are Heliocentric and in km s^{-1}. LSR values are 18.2 less. Parentheses indicate the reduced number of spectra.
[b] Ratios group around these values.
[c] One Large Sample only.

that appears to be free of this extra extinction. The results for these samples are repeated in Table 4 under the headings "SW Control" and "SW Cloud." We examine the properties in the three regions and their nearby low extinction areas in order to assess the effects of the extinction and what it can tell us about the structure along the LOS.

The primary comparison regions for the Dark Bay are the −90″ Profile Central sample and the SE Region. For the Ori-S Cloud, the NE Region and SW-Regions are useful for comparison. These pairings are in addition to the SW-Cloud and SW-Control Regions. The results for all of the pairings are shown in Table 4.

In the Dark Bay, we see a large jump in $S_{\rm mif,[N\ II]}/S_{\rm mif,[O\ III]}$, which is compatible with the high extinction there. We probably do not see a $V_{\rm low,[O\ III]}$ component in the −90″ Dark Bay sample because the large FWHM (19.4 ± 0.6 km s^{-1}) of the $V_{\rm mif,[O\ III]}$ component makes it undetectable on the shoulder of the $V_{\rm mif,[O\ III]}$ component. Four of the six Dark Bay $V_{\rm mif,[N\ II]}$ components are very wide (FWHM = 23 ± 2 km s^{-1}). This indicates that it is a blend with another velocity component or that we are seeing a blend of extincted $V_{\rm mif,[N\ II]}$ emission and emission arising from the near side of the Dark Bay. These same factors could also lead to the jump in $V_{\rm mif,[N\ II]}$ above the Control and SE Region. Similar considerations may explain the jump in $V_{\rm low,[N\ II]}$, although the rise may be an artifact of extracting the $V_{\rm low,[N\ II]}$ from the shoulder of the unusually wide $V_{\rm mif,[N\ II]}$ component.

In the Orion-S Cloud, there is only a marginal indication of a rise in $S_{\rm mif,[N\ II]}/S_{\rm mif,[O\ III]}$, as expected since the extinction is occurring within the Cloud, and we see the foreground side of the Cloud. Unfortunately, only one Large Sample record $V_{\rm low}$ components, so no meaningful comparison can be made of these with their surroundings.

In the SW Cloud, $S_{\rm mif,[N\ II]}/S_{\rm mif,[O\ III]}$ rises to 1.7 ± 0.1, well above the SW Control region of 1.1 ± 0.2, and indicating high extinction, although not as great in the Dark Bay. $S_{\rm low,[N\ II]}/S_{\rm mif,[N\ II]}$ is the same as in the nearby SW Control samples and the SW Region. $S_{\rm low,[O\ III]}/S_{\rm mif,[O\ III]}$ is compatible with one of the unexplained groupings in the SW Region and in the SW Control samples.

We note that there is a general decrease in $V_{\rm mif}$ proceeding from the NE to the SW across of the Huygens Region. This is quite smooth for $V_{\rm mif,[N\ II]}$, while $V_{\rm mif,[O\ III]}$ drops abruptly at the Orion-S Cloud. $S_{\rm low}/S_{\rm mif}$ ratios are usually the same (within their probable errors) in the dark samples and their comparison regions. This indicates that the layer producing the $V_{\rm low}$ components (the NIL) lies between θ^1 Ori C and Veil components B and C that cause the extinction.

6. Development of a 3D Model for the Line of Sight near the Trapezium

Understanding the structure along an LOS from the observer to the PDR requires using all the data in hand, plus computational modeling. Through these, we have developed a 3D model.

6.1. Refinement of the θ^1 Ori C–NIL Photoionization Model Distance

In Abel et al. (2019), photoionization models were calculated for the NIL over a wide range of distances from θ^1 Ori C and the density of the layer. These were then used to predict the surface brightness in the [N II] and [O III] emission lines and the column density of He I in the lowest triplet state (2^3S, designated as He I*), where the 388.9 nm absorption line arises that appears in the spectra of the Trapezium stars. We repeated those calculations using an improved determination of the 388.9 nm line and the surface brightness in [N II] in addition to dropping modeling of the [O III] line.

Abel et al. (2019) used the observed equivalent width of the 388.9 nm line from the brightest four Trapezium stars to derive an average column density N(He I*, cm^{-2}). We now think it is better to use only the observations of θ^1 Ori A, θ^1 Ori C, and θ^1 Ori D since the 388.9 nm absorption line in θ^1 Ori B is clearly affected by the nearby He I and H8 emission lines. The average of the three stars is (1.45 ± 0.17) × 10^{13} cm^{-2} with a better defined uncertainty.

We have used a higher value of the surface brightness of [N II] based on artificial models of the emission line, as done in Appendix A, except that we have specifically used FWHM (16.6 ± 1.4 km s^{-1}), $V_{\rm mif,[N\ II]}$–$V_{\rm low,[N\ II]}$ (15.3 ± 1.3 km s^{-1}), and $S_{\rm low,[N\ II]}/S_{\rm mif,[N\ II]}$ (0.07 ± 0.02) from nine Large Samples surrounding θ^1 Ori B (the star used to derive the ultraviolet absorption lines). These models established that the true $S_{\rm low}/S_{\rm mif}$ is 1.4 times larger than derived from "spcflot."

We have not modeled the [O III] line because $V_{\rm low,[O\ III]}$ is not usually present; therefore, the few available values do not give an accurate constraint on the models. As a result, we have one less constraint on the model of the NIL than in Abel et al. (2019), but the [N II] and He I* constraints are now better defined and more reliable.

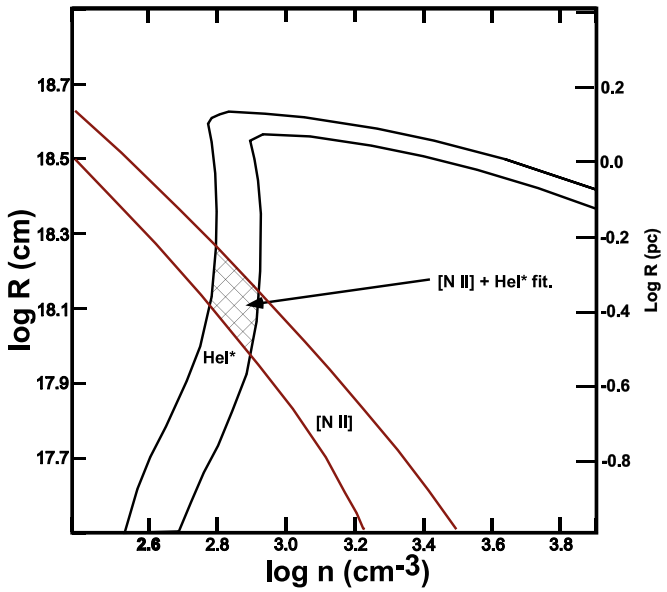

Figure 6. This plot of log n (cm^{-3}, the density of hydrogen atoms) versus the separation of θ^1 Ori C and the NIL is similar to Figures 4–6 in Abel et al. (2019), except that a larger range of density and distances is used, and we have dropped modeling of [O III]. In addition, improved accuracy of the He I* and [N II] observational constraints was utilized. The red lines enclose the range of values where the photoionization models match the observed surface brightness of $V_{low,[N\,II]}$. The black lines include the range consistent with the observed value of the column density of He I*. The cross-hatched region indicates where there is agreement of the [N II] and He I* data, as discussed in Section 6.1.

We see the results of the comparison of the predictions and observations in Figure 6. The combination of brighter [N II] emission and a 30% higher He I* column density yields a model with nearly the same density as in Abel et al. (2019) but about half the distance from θ^1 Ori C. There is a single overlapping zone of allowable fits of the observations and the predictions, shown as a cross-hatched region in Figure 6. The Central value is Log $R = -0.39$ (0.41 pc) and Log $n = 2.84$ (690 cm^{-3}). The allowable range of log R is -0.22 (0.60 pc) to -0.52 (0.30 pc) and the allowable range of Log n is 2.79 (620 cm^{-3}) to 2.91 (790 cm^{-3}).

The 2^3S state is populated by recombinations of singly ionized helium, and this region also produces the [O III] emission, but not [N II] emission. This means that a caveat on our conclusions is that the 388.9 nm records the $He^+ + H^+$ zone and the [N II] line the $He^o + H^+$ zone. Without a detailed model of the ionization structure of the NIL, we cannot quantitatively assess how this could affect our results. However, we expect the effects to be small.

6.2. Relative Positions of the NIL and the Orion-S Cloud in Earlier Studies

The distance between the blueshifted collimated outflows from the Orion-S Cloud and material with which it collides has been treated in multiple earlier studies, some predating knowledge of the the NIL.

In their study of HH 203 and HH 204 that lie to the southeast from the Bright Bar, Doi et al. (2004) calculated the angles of the flow from the Orion-S Cloud and determined foreground displacements of the shocked material at 0.2 pc and 0.3 pc, respectively, coming to the conclusion that these shocks were the result of jets originating from the Orion-S Cloud shocking material in the MIF in the region immediately southeast of the Bright Bar. They accepted this geometry because the NIL was not recognized at that time, the MIF was known to curve toward the observer at the Bright Bar, and estimates of the Veil atomic components distances were much larger. With the recognition of the NIL, it is more likely that this is NIL material, shocked by the SE outflows from the Orion-S Cloud.

van der Werf et al. (2013) associated the Veil H I absorption feature F with the well-studied flow and shocks defining HH 202 (that lies to the NW from the Orion-S Cloud) and concluded that the Veil lay 0.26 pc (corrected to our distance of 383 pc) toward the observer from the Orion-S Cloud. They did not consider the existence of the NIL. In Abel et al. (2016), we established that the H_2 absorption spectrum along with the neutral carbon absorption spectrum in the UV makes it impossible for Veil component B to be this distance from the Cloud and therefore the Trapezium. The present work reconciles Abel et al. (2016) with van der Werf et al. (2013). There is a dynamical interaction between the layers in front of the Trapezium and HH 202, but the interaction is not with Veil Component B, but with the NIL.

In the context of the present study, we note that absorption feature F shows two velocity peaks at -1 and $+7$ km s^{-1} (both Heliocentric) and that these fall into the range of velocities encountered in the NIL. Linking an H I absorption line area to a small region in the ionized NIL is plausible by assuming mass loading at the front of the flow followed by rapid recombination of ionized hydrogen. This was predicted in the models for Herbig–Haro shocks by Hartigan et al. (1987). Abel et al. (2016) argue that the association of HH 202 and absorption feature F is incorrect, presenting several arguable if not hard and fast reasons that HH 202 and absorption feature F are not associated. They do not consider that a neutral zone can be formed at the head of a shock.

If one accepts that the HH 202, HH 203, and HH 204 shocks occur in the nearest foreground layer, this would mean that the NIL is about 0.2–0.3 pc in front of the Orion-S Cloud, the host of multiple stellar outflows. The distance in front of θ^1 Ori C would depend on the separation of θ^1 Ori C and the Orion-S Cloud along the LOS.

6.3. Probable Spacings of θ^1 Ori C, the Orion-S Cloud, and the NIL

The position of the features along an LOS near the Trapezium can be determined from multiple lines of evidence. Even though each of these methods has an uncertainty because of assumptions made in each, together they give a self-consistent explanation of the positions. The model presented is an improvement over previous efforts (O'Dell et al. 2009; O'Dell & Harris 2010).

Figure 7 shows the results for derivation of differences in position along the LOS. The distances are relative to θ^1 Ori C and different methods of deriving distances are color coded.

The θ^1 Ori C–MIF distance (black lines) in Figure 7 was taken from O'Dell et al. (2017) and is based on the relative surface brightness of [N II] and [O III] near θ^1 Ori C. O'Dell et al. (2017) adopted a distance of 0.15, which is smaller than obtained from surface brightness in hydrogen recombination lines. The dashed black lines show the possible range of values of this distance.

The radius of the High Ionization Arc (green lines) is taken to represent the boundary of the Central Bubble, the range in

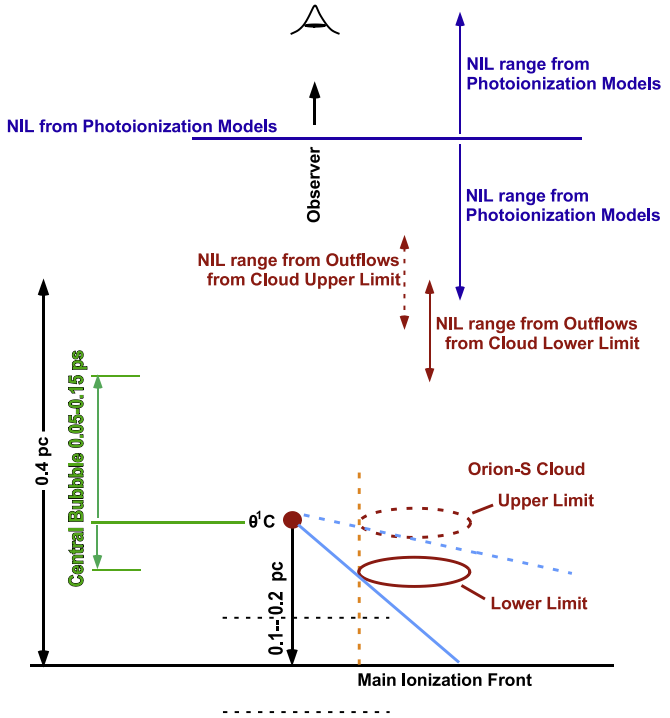

Figure 7. This working image shows the possibilities for the relative location of the MIF, θ^1 Ori C, the Orion-S Cloud, the boundary of the Central Bubble, and the NIL along an LOS through θ^1 Ori C (the red filled circle) as discussed in Section 6.3.

distances reflects the fact that the Central Bubble may be noncircular, and we have noted that the effects of the Central Bubble extend beyond the High Ionization Arc.

The blue lines represent the θ^1 Ori C–NIL distance derived in Section 6.1 from a photoionization model. The heavy blue line represents the center of the fitted region in Figure 6, while the dashed blue lines indicate the extreme values of the fitted region.

Red is used to indicate features related to the Orion-S Cloud. The position of the Cloud is constrained laterally by the separation between θ^1 Ori C and the NW tilted boundary of the Cloud (33″, 0.061 pc, the orange dashed line in Figure 7). However, a range of values along the LOS for the Cloud can be derived from considerations of ionization of MIF material behind or shadowed by the Cloud, in addition to the Cloud's degree of ionization.

The Orion-S Cloud is sufficiently optically thick that it contains H_2CO and H I, conditions that determine that it must be optically thick in Lyman continuum ionizing photons (LyC). This means that there will be a LyC shadow beyond the Orion-S Cloud. Where this shadow strikes the surface of the OMC, the MIF surface brightness will be low but not zero since these regions will be illuminated by the diffuse LyC radiation field created by recombining gas. This shadowed region will be further from θ^1 Ori C as the distance between the Orion-S Cloud and the MIF is increased.

It is possible that there are regions of the MIF that are directly illuminated by θ^1 Ori C but hidden along the observer's LOS to the Orion-S Cloud. One sees H_2CO and H I absorption lines against an ionized gas continuum in the direction of the Cloud. This means that a region beyond (further from the observer) but in alignment with the Cloud, is directly illuminated by θ^1 Ori C. This restricts the minimum MIF–Cloud distance to 0.1 pc, as shown in the solid red line ellipse and solid light-blue line in Figure 7.

The Cloud could be even closer to the observer, allowing ionization of MIF material well beyond (away from θ^1 Ori C) the Cloud. However, an upper limit to this distance is when the θ^1 Ori C–MIF and Cloud-MIF distances are equal. Beyond that, the nearer (to the observer) side would not be ionized by θ^1 Ori C, in conflict with the fact that the near side of that Cloud is ionized. This upper limit is shown by the dashed red ellipse and dashed light-blue line in Figure 7. This means that the lower limit of the separation is about 0.1 pc and the upper limit about 0.15 pc.

In Section 6.2, we established from outflows from the Orion-S Cloud that strike the NIL that their separation is 0.2–0.3 pc. Figure 7 shows where this would place the NIL with respect to the two limits of the Cloud-MIF.

The overall arrangement and scale of distances is satisfactory as it places the NIL at 0.4 pc in the same region from multiple approaches. It is attractive (Section 7.2), as it satisfies the condition for the Central Bubble to be inside the NIL.

Of course, all of this structure falls well within the distances (Abel et al. 2019) of 2.0 pc for Veil component B and 4.2 pc for Veil component A.

7. Discussion

7.1. The Central Bubble

We interpret the High Ionization Arc to be the boundary in the plane of the sky of the Central Bubble surrounding the Trapezium stars. This cavity was originally proposed in a low spatial resolution (0′.9) radio map in H76α by Pankonin et al. (1979) but did not receive much attention until the optical study in O'Dell et al. (2009), where its properties were discussed in detail as the product of a hot, shocked, wind-blown cavity driven by the strong stellar wind from θ^1 Ori C (Howarth & Prinja 1989; Gagné et al. 2005). Arthur (2012) modeled the properties of such a cavity while trying to explain the observed region of cool X-ray emitting gas found in the EON (Güdel et al. 2008). She established that a central cavity of hot shocked gas was a natural product of the stellar wind and that an opening in it could produce the EON X-ray emitting material. X-ray emission should also occur in the region surrounding θ^1 Ori C, but that emission is absorbed by the foreground layers of the Veil.

Figure 1 shows that our Large Samples in the NE Region fall within the [O III] feature that defines the inner boundary of the High Ionization Arc. Immediately east of θ^1 Ori C, the arc has a north–south diameter of 110″, corresponding to 0.2 pc. In contrast, the SW-Region data mostly come from a region where the High Ionization Arc is open, with the Orion-S Cloud in the direction of the opening. The SE-Region lines close but outside the SE boundary of the High Ionization Arc.

Following Abel et al. (2019), we attribute the $\boldsymbol{V}_{\rm new}$ components (Section 4.3) to emission from the far (away from the observer) side and the $\boldsymbol{V}_{\rm blue}$ components (Section 4.3) to emission from the nearer side of the Central Bubble.

In Figure 5, we see that the far-side $\boldsymbol{V}_{\rm new}$ components are most frequently found in the SW Region, appearing there with equal frequency in $\boldsymbol{V}_{\rm new,[N\ II]}$ and $\boldsymbol{V}_{\rm new,[O\ III]}$. This difficult-to-detect component is seen in [O III] in both the SE and NE-Regions, and only four times in [N II] in the NE Region. The presence of $\boldsymbol{V}_{\rm new,[O\ III]}$ outside of the High Ionization Arc can be

used as an argument against this component occurring within the Central Bubble as presented in Section 5.2 of Abel et al. (2019). However, the optical feature is likely to simply be the sharp edge of a more extended shell.

We also see in Figure 5 that the $V_{\rm blue,[N\ II]}$ components are common in the NE and SW Regions, while these Regions contain fewer $V_{\rm blue,[O\ III]}$ features. The SE Region is almost free of $V_{\rm blue}$ components except for three Large Samples including $V_{\rm blue,[N\ II]}$. The frequency and distribution of the $V_{\rm new}$ components argue for their being formed on the facing side of the Central Bubble.

In Section 4.3, we found that $V_{\rm blue,[N\ II]}$ appears in 21 NE-Region Large Samples with an average of -6 ± 3 km s^{-1} and in 11 SW-Region Large Samples with an average of -4 ± 3 km s^{-1}, for a weighted average of -5 ± 3 km s^{-1}. $V_{\rm blue,[O\ III]}$ appears in five times in the NE Region with an average of 1 ± 4 km s^{-1} and ten times in the SW region with an average of -1 ± 5 km s^{-1}, for a weighted average of -1 ± 4 km s^{-1}.

In Section 4.3, we also found that $V_{\rm new,[N\ II]}$ appears in four NE-Region Large Samples with an average of 37 ± 12 km s^{-1}. It is much more abundant in the SW-Region Large Samples (appearing 26 times with an average of 33 ± 2 km s^{-1}). The weighted average of both regions is $V_{\rm new,[N\ II]} = 34 \pm 1$ km s^{-1}. $V_{\rm new,[O\ III]}$ appears 13 times in the NE-Region Large Samples (with an average of 27 ± 5 km s^{-1}) and 20 times in the SW Region (with an average of 27 ± 8 km s^{-1}). It is also seen seven times in the SE-Region with an average of 27 ± 2 km s^{-1}. The weighted average is $V_{\rm new,[O\ III]} = 27.0 \pm 5$ km s^{-1}.

These velocities indicate that the boundaries of the Central Bubble are rapidly expanding. The side approaching the MIF is slowed by gas photoevaporating from the MIF with the $V_{\rm new,[N\ II]}$ component moving away from θ^1 Ori C (assumed to be at 25 km s^{-1} (Sicilia-Aguilar et al. 2005)) at 9 km s^{-1} and the $V_{\rm new,[O\ III]}$ component essentially at 2 km s^{-1}.

The side approaching the observer is moving away from θ^1 Ori C at relative velocities of 30 km s^{-1} for [N II] and 26 km s^{-1} for [O III].

7.2. Relation of the Blueshifted Central Bubble Velocities and the NIL Velocities

The source of the blueshift of the NIL is most likely to be the blueshifted side of the expanding Central Bubble, which we saw in Section 7.1, is approaching the observer at $V_{\rm blue,[N\ II]} = -5 \pm 3$ km s^{-1} and $V_{\rm blue,[O\ III]} = -1 \pm 4$ km s^{-1}. Given that the characteristic NIL velocities are $V_{\rm low,[N\ II]} = 5 \pm 3$ km s^{-1} and $V_{\rm low,[O\ III]} = 8 \pm$ km s^{-1}, this means that the nearer side of the Central Bubble are approaching the NIL at 10 ± 4 km s^{-1} and 9 ± 4 in [N II] and [O III], respectively.

7.3. Colliding Features along the LOS

In our study of the many different features in the central Huygens Region, we have found that everything is moving relative to one another. We summarize these results in Figure 8.

The closure time for the near side of the Central Bubble to the NIL is very short; in fact, we may already be seeing a case where the fast-moving gas is pushing against the denser NIL. The closure time between the NIL (at 0.4 pc and 6 ± 2 km s^{-1}) and the Veil B component (at 2.0 pc and 19 ± 1 km s^{-1} from Abel et al. (2019) is 1.2×10^5 yr, longer than the estimate of 30,000–60,000 yr in O'Dell (2018).

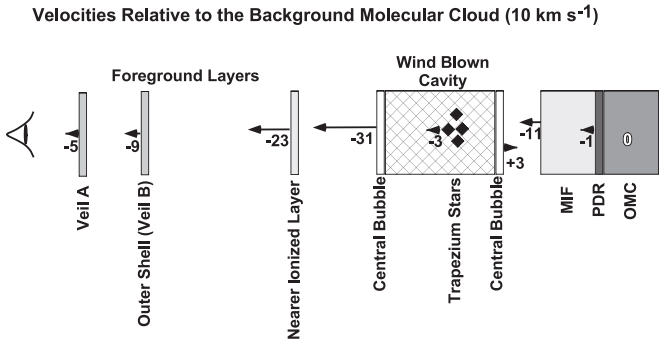

Figure 8. The positions (not to scale) and velocities relative relative to the OMC are shown and discussed in Section 7.3. This is an updated version of Figure 9 in Abel et al. (2019).

7.4. The Nature of the Scattering Particles

In Table 2, we see that there is good agreement of the expected (isotropic scatterers) and observed velocity differences under the assumption of $V_{\rm mif}$ being the source of the light that is backscattered.

This difference in the $V_{\rm scat}$–$V_{\rm mif}$ values can inform the question of the nature of the scattering properties of the particles in the PDR. If the backscattered light was strongly concentrated back along the incoming beam, looking along a perpendicular tilted region would give a very weak $V_{\rm scat}$ component and its velocity would $V_{\rm PDR}$, that is, the same as the observed $V_{\rm mif}$, so that $V_{\rm scat}$–$V_{\rm mif} = 0$. If the particles were isotropic scatterers, the observed $V_{\rm scat}$–$V_{\rm mif}$ would be the usual flat region value $2 \times V_{\rm evap}$. The fact that the data shown in Table 2 are in good agreement with expectation is a strong argument that the scattering particles are nearly isotropic scatterers. However, the closeness to true isotropy depends on the accuracy of our approximation that the velocity shift should be $2 \times V_{\rm evap}$.

7.5. The Putative Relation of the $V_{\rm low}$ and $V_{\rm mif}$ Components

In O'Dell (2018), it was argued that there is an approximately linear correlation between the $V_{\rm low}$ and $V_{\rm mif}$ components. The $V_{\rm low}$ component is always close to the $V_{\rm mif}$ component (about 13–18 km s^{-1}) and thus difficult to measure, because it is seen as a small signal on the blue shoulder of the strong $V_{\rm mif}$ component. The conclusion in O'Dell (2018) was that $V_{\rm mif}$–$V_{\rm low}$ is 18 km s^{-1} for [N II] and 13 km s^{-1} for [O III].

Abel et al. (2019) demonstrated that the linear correlation is very dependent on the mix of data employed. The O'Dell (2018) study used data from both the Large Samples near the NE Region and the results from lower S/N individual slits. They argue that the correlations becomes questionable if one only uses the Large-sample results. These cautions advise reassessing the relation using the full data set in the current study.

We have used the Regions spectra to assess the likelihood of a correlation of $V_{\rm low}$ and $V_{\rm mif}$. These represent the highest S/N set of data available and they have identifiable probable errors. Figure 9 was created using data from Table 1. In this figure, we see several features.

The [N II] values cluster around $V_{\rm mif,[N\ II]}$–$V_{\rm low,[N\ II]} = 16.5 \pm 3.0$ km s^{-1} with an indication of a linear relation with a displacement of 16.5 ± 2 km s^{-1}. A more apparent linear correlation of $V_{\rm low,[O\ III]}$–$V_{\rm mif,[O\ III]}$ appears with a shift $V_{\rm mif,[O\ III]}$–$V_{\rm low,[O\ III]} = 11.5 \pm 2$ km s^{-1}. The apparent correlations disappear if one disregards the SW-Region points. This would be

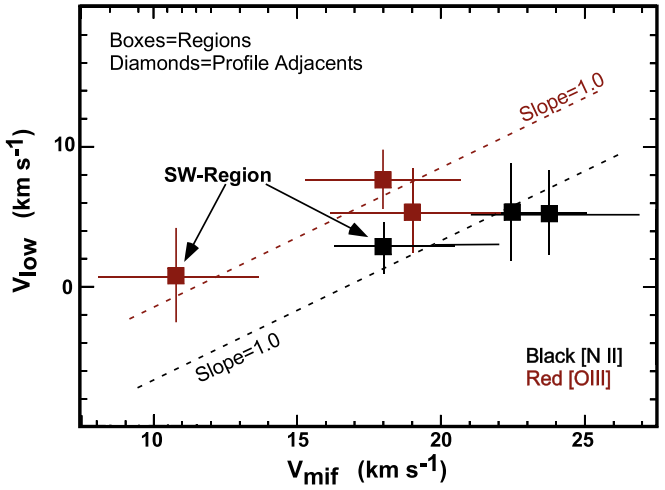

Figure 9. The possible correlation of V_{mif} and V_{low} is illustrated in this figure. It is similar to Figures 4 and 5 of O'Dell (2018) but more definitive as we now only use larger samples of higher S/N ratio in addition to showing probable errors. We identify the values for the SW Region, which is affected by the Orion-S Cloud.

justified since that region has anomalous values of many features, and it is discussed in detail in Paper II.

Rather than a correlation between the V_{mif} and V_{low} velocities, an alternate view is that V_{mif} varies because of differences in the inclination of the MIF, while V_{blue} varies according to selection effects in analyzing the spectra. Previously, we have argued that the apparent correlation of velocities is real (O'Dell 2018; Abel et al. 2019), but the current assessment indicates that they are associated with the intrinsic properties of the nebular lines and our method of analysis.

We expect V_{mif} to vary according to the inclination of the MIF that produces it. For a flat-on MIF, V_{mif} would be V_{PDR}–V_{evap}, 20 km s^{-1} and 15 km s^{-1} for [N II] and [O III], respectively. V_{mif} for an edge-on MIF would be the V_{PDR} value of 27 km s^{-1}. The V_{mif} components shown in Figure 9 are consistent with this expectation except for the SW Region $V_{mif,[O\ III]}$ of 11 ± 3 km s^{-1}.

In Section 4.2, we saw that there is a host of data that argue for a constant V_{low} of 5 ± 2 km s^{-1}, which is consistent with the V_{low} results shown in Figure 9, after consideration of the probable errors of their determination. The outlying sample is $V_{low,[O\ III]} = 1 \pm 3$ for the SE Region. In a separate publication, we will show that the [O III] emission in the SW Region is highly irregular.

After consideration of the above material and the fact that the apparent V_{mif}–V_{low} values lie close to the limits imposed by the FWHM of the V_{mif} components, we must conclude that there is not a causal relation between the V_{mif} and V_{low} velocities.

7.6. Magnetic Fields in the Huygens Region

In a recent study from the Stratospheric Observatory for Infrared Astronomy, Chuss et al. (2019) measured the polarization at multiple wavelengths of infrared continuum emission arising from dust in the Huygens Region. This radiation can arise from a heated imbedded region such as the active BN–KL region or from the high-density PDR dust that is heated by radiation from the bright stars near the center of the Orion Nebula Cluster. Their observations at 53 μm provided the highest angular resolution (5.″1), and at this wavelength, they find $B = 1000$ μG for the BN–KL Region and 261 μG for a quiescent region. The latter number is much larger than the characteristic average of 56 μG found in the foreground Veil A component by Troland et al. (2016).

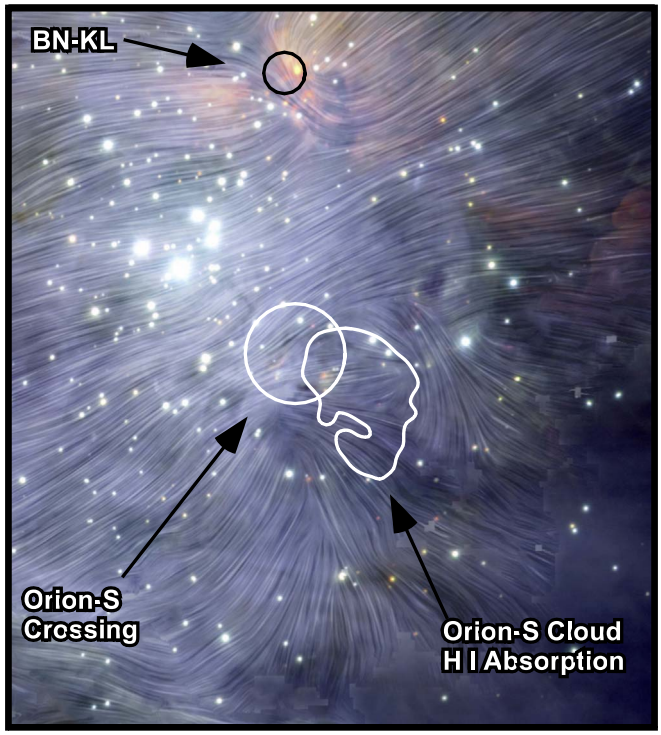

Figure 10. This 194″ × 216″ (0.36 × 0.39 pc) infrared image of the Huygens Region (a portion of an European Southern Observatory press release 2001 January 19) has superimposed the magnetic field directions in the plane of the sky determined by Chuss et al. (2019) from polarized 53 μm PDR dust emission at 5.″1 resolution (Astronomy Picture of the Day 2019 February 27). The location of the BN–KL imbedded complex of young stars is shown, as are the boundaries of the Orion-S Cloud as determined from H I 21 cm absorption lines (van der Werf et al. 2013), and the Orion-S Crossing.

7.6.1. Magnetic Field Directions near BN–KL and the Orion-S Cloud

Figure 10 is a cropped segment of an infrared image with the Chuss et al. results superimposed. It shows that in this area, the direction of the magnetic field at 53 μm usually varies only slowly with position with the exception of the BN–KL region and the Orion-S Cloud. The variations in the BN–KL region are discussed in detail in Chuss et al. (2019) but not the Orion-S Cloud properties, which are emphasized in our discussion.

The region around the Orion-S Crossing and the Orion-S Cloud has properties obviously relevant to the local structure. Figure 1 of Chuss shows that the magnetic field is weaker than average in the inner parts of what we designate as the SW Region, and our Figure 10 shows that the large-scale direction of the magnetic field in the SW Region is perpendicular to that in the center of the Huygens Region. The local peak surface brightness at 53 μm occurs near the center of the Crossing. Evidently, the PDR producing the 53 μm radiation is of a very different geometry than the surrounding nebula. In addition, the direction and lower strength of the field then extends into the SW Region. This strengthens our argument that this region is different from other parts of the Huygens Region and the argument that the cause of the difference lies with the Orion-S

Cloud and its NE corner, which is strongly illuminated by θ^1 Ori C. These are elaborated upon in Paper II.

7.6.2. A Connection of Different Regions through Ambipolar Diffusion?

Given the wealth of information on the Orion complex, it is possible to compare the magnetic field and density for different regions of Orion. Crutcher (1999) found, from 27 Zeeman observations of molecular clouds, a relationship between magnetic field strength and density, $B \propto n^{0.47}$. This result is consistent with ambipolar diffusion-driven star formation, where the magnetic field-density relation would be given by $B \propto n^{0.5}$. Given the known magnetic field and density in the neutral layers of the Veil, we can calculate the expected density in BN–KL and the H II region based on the relation from Crutcher (1999). For Veil component A, $B \simeq 56\ \mu$G (Troland et al. 2016), and the density is $10^{2.4}$ cm^{-3} (Abel et al. 2016). Using these values, the magnetic field of BN–KL yields a density of $10^{5.1}$ cm^{-3}, and the H II region gives a density of $10^{3.8}$ cm^{-3}. These densities are very close to the densities derived from PDR modeling in Morris et al. (2016) of $10^{5.3}$ cm^{-3} (for BN–KL) and of $10^{3.8}$ cm^{-3} (for the H II region; Baldwin et al. 1991). This argues for the possibility that ambipolar diffusion is a physical process connecting multiple regions of Orion, such as the Veil and BN–KL, even though their physical separation exceeds 2 parsecs.

7.7. A Recent Study of the Veil B [C II] Component

In a recent paper, Pabst et al. (2019) reported mapping a 1° field around the Huygens Region in the [C II] 158 μm line at 0.2 km s^{-1} and 16″ resolution. They identified a curved shell of about 2500″ (41.′7) diameter (4.6 pc at 383 pc distance) and a maximum expansion velocity toward the observer of 13 km s^{-1}. We'll refer to this as the Outer Shell. They then modeled this feature as a 2 pc diameter bubble and explained its structure and dynamics as the result of the hot gas (Güdel et al. 2008) created by reverse shocks from the stellar wind sweeping up surrounding gas and forming a shell.

The discovery of the Outer Shell is an important step in understanding the EON. A draft of a longer paper expanding upon Pabst et al. (2019) shows that the Outer Shell velocity near the Trapezium is 19 km s^{-1} while the component associated with the background PDR is at 28 km s^{-1}.

This portion of the Outer Shell in the direction of the Huygens Region has previously been studied, before the recognition of the Outer Shell. It was discovered in the 21-cm H I absorption line study of van der Werf & Goss (1989) as component Veil B at 19.4 km s^{-1}, seen in H_2 ultraviolet absorption lines at 19.5 ± 0.7 km s^{-1} (Abel et al. 2016) and seen in Ca II and Na I optical absorption lines at 18.3 km s^{-1} and 19.8 km s^{-1}, respectively (O'Dell et al. 1993), and additionally seen at 19 ± 2 km s^{-1} in [C II] (Goicoechea et al. 2015) using the same emission line (0.2 km s^{-1} and 11.″4 resolution). These velocities were summarized in Table 2 of Abel et al. (2019). The weighted average of the components is 19.2 ± 0.5 km s^{-1}.

There remains an open question of how to reconcile the results of this study (which argues that the stellar wind escapes the Central Bubble only to the SW) and the fact that the Outer Shell extends across and slightly north of the Trapezium.

8. Conclusions

1. θ^1 Ori C is surrounded by a wind-blow Central Bubble open to the SW and about 110″ (0.21 pc) north to south width at the star.
2. There is a layer of ionized gas (the NIL) extending across the Huygens region. At 0.4 pc from θ^1 Ori C, it lies just outside the Central Bubble.
3. The dust particles in the PDR are isotropic back-scatterers.
4. A previously proposed relation between $\boldsymbol{V}_{\rm mif}$ components arising from the MIF and $\boldsymbol{V}_{\rm low}$ components arising from the NIL is shown to be unlikely. Its appearance is primarily due to the difficulty of measuring a weak line on the shoulder of the $\boldsymbol{V}_{\rm mif}$ component.
5. The Veil B components, seen in H I and multiple ions appear to be part of an Outer Shell discovered in high-velocity resolution mapping of the EON.
6. Our SW-Region sample has unusual $\boldsymbol{V}_{\rm mif,[O\ III]}$ properties and is located in a region where the PDR's magnetic field orientation and strength is different from other parts of the Huygens Region (with the exception of the area near the BN–KL objects).

We are grateful to C. H. M. Pabst of Leiden University for sharing a draft of her paper expanding upon Pabst et al. (2019), discussions on the Outer Shell, and her comments on a draft of this paper. The observational data were obtained from observations with the NASA/ESA *Hubble Space Telescope*, obtained at the Space Telescope Science Institute, which is operated by the Association of Universities for Research in Astronomy, Inc., under NASA Contract No. NAS 5-26555; the Kitt Peak National Observatory and the Cerro Tololo Interamerican Observatory operated by the Association of Universities for Research in Astronomy, Inc., under cooperative agreement with the National Science Foundation; and the San Pedro Mártir Observatory operated by the Universidad Nacional Autónoma de México. G.J.F. acknowledges support by NSF (1816537, 1910687), NASA (ATP 17-ATP17-0141), and STScI (HST-AR- 15018).

Appendix A
The Visibility of the V_{low} Component is Determined by the FWHM of the V_{mif} Component

It is prudent to examine if the $\boldsymbol{V}_{\rm low}$ results are due to the manner in which the spectra were analyzed. In Appendix A of O'Dell (2018), it was illustrated how artificially created spectra closely resemble the observed spectra, using the [N II] line for the comparison. However, this illustration does not critically test the visibility of the $\boldsymbol{V}_{\rm low}$ component. It is intuitively obvious that if the $\boldsymbol{V}_{\rm mif}$ component is broad, it will be difficult to find a weak $\boldsymbol{V}_{\rm low}$ component on its blue shoulder. The tests we describe below are intended to quantitatively evaluate the limits of detection of the $\boldsymbol{V}_{\rm low}$ component.

A series of model spectra were created using varying relative strengths and displacements of the $\boldsymbol{V}_{\rm low}$ components. These were created by adding the $\boldsymbol{V}_{\rm low}$ components to a fixed spectrum composed of a $\boldsymbol{V}_{\rm mif}$ component with a variable FWHM plus a $\boldsymbol{V}_{\rm scat}$ component of FWHM = 22 km s^{-1} and displaced 20 km s^{-1} to the red. These were called the RED spectra. A series of RED spectra were created with $\boldsymbol{V}_{\rm mif}$ FWHM values of 10, 12, 14, and 16 km s^{-1}. For each of these, a series of $\boldsymbol{V}_{\rm low}$ spectra were added, with the same FWHM for $\boldsymbol{V}_{\rm low}$ and varied assumed values of $\boldsymbol{S}_{\rm low}/\boldsymbol{S}_{\rm mif}$. This process should test whether a grouping of $\boldsymbol{V}_{\rm low}$–$\boldsymbol{V}_{\rm mif}$ values as shown in Figure 9 are

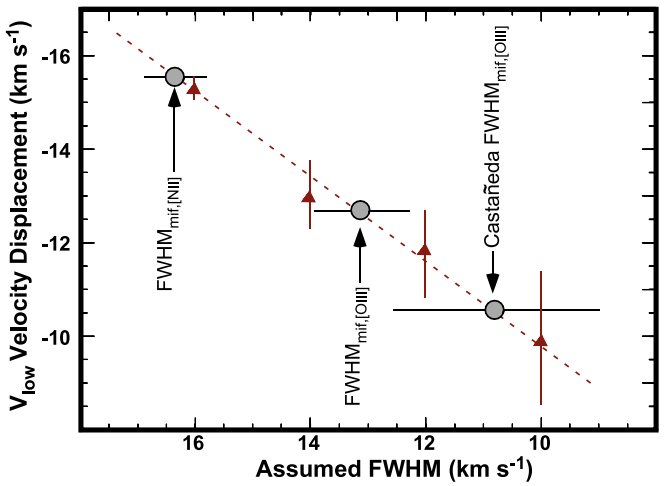

Figure 11. The red triangles show the minimum measurable velocity displacement for V_{low} components as a function of the FWHM of the V_{mif} components (V_{low} is assumed to the the same) for the models explained in Appendix A. The dispersion in the measured V_{low} displacements is from five independent deconvolutions using "splot" for each limiting detection spectrum. V_{low} components above the dashed red line should be clearly measured in actual spectra of a specific FWHM. The large gray filled circles indicate the average FWHM of the MIF component in our study and in the higher-resolution study of Castañeda (1988) of [O III].

a product of the analysis of the data, rather than revealing a true correlation.

It was found that at a fixed FWHM and diminishing values of S_{low}/S_{mif}, a point was reached where the V_{low} component had disappeared from visibility in the blue wing of the composite spectrum. That point was set at the same level of visibility employed in the measurement of the nebular spectra. Larger displacements than this limit would have been clearly identified and measured. Below that point, no V_{low} component would have been measured. The results are shown in Figure 11 as red triangles.

The limiting V_{low} values in Figure 11 fall along an indistinguishably linear relation (shown as a red dashed line) with the limiting velocity being slightly less than the assumed FWHM. This figure also shows the average FWHM of the $V_{mif,[N\,II]}$ and $V_{mif,[O\,III]}$ values in the Regions. When those FWHM values are shifted to lie on the dashed red line, they should indicate the minimum displacement of the V_{low} component that can be measured.

Nearly all of the nebular spectra $V_{mif,[N\,II]}$ components (FWHM $= 16.4 \pm 0.6$ km s^{-1}) had detectable $V_{low,[N\,II]}$ components, while only some of the $V_{mif,[O\,III]}$ components did (FWHM $= 13.2 \pm 0.8$ km s^{-1}).

At the average FWHM of the $V_{mif,[N\,II]}$ components, the expected minimum $V_{low,[N\,II]}$ shift would be -15.5 ± 0.5 km s^{-1}. At the average of the $V_{mif,[O\,III]}$ components with $V_{low,[O\,III]}$ components, the expectation is -12.7 ± 0.8 km s^{-1}. As discussed in Appendix A, the observed $V_{low,[N\,II]}$ components lie in a region relatively unaffected by the process of its identification, but the $V_{low,[O\,III]}$ components are affected. In the latter case, we draw on the results of the higher-resolution study of [O III] by Castañeda (1988).

Appendix B
Revisions to the LOS Table Presented in Abel et al. (2019)

Table 2 of Abel et al. (2019) summarized the velocities of various velocity components, using data from their study and previously published material. Our study has doubled the number of spectra, and we have revised portions of that table, creating Table 5. We now use the term NIL instead of the previous Ionized Component I.

Table 5
Velocity Systems

Designation	Component and Velocity (km s^{-1})	Source
NIL	(6 ± 2)	Weighted Average
…	$V_{low,[N\,II]}$ (5 ± 3)	All three Regions
…	$V_{low,[O\,III]}$ (8 ± 3)	Castañeda (1988)
…	[O II] (system B, 3.1)	Jones (1992)
…	[S III] (system B, 9.9)	Wen & O'Dell (1993)
…	He I (absorption, 2.1 ± 0.6)	O'Dell et al. (1993)
…	P III (absorption, 4.9 ± 3.0)	Abel et al. (2006)
…	S III (absorption, 4.5 ± 0.9)	Abel et al. (2006)
…	Ca II[a] (absorption, 7.5)	O'Dell et al. (1993)
…	Na I[b] (absorption, 6.0)	O'Dell et al. (1993)
Nearer Central Bubble	$V_{blue,[N\,II]}(-5 \pm 3)$	Two Regions
…	$V_{blue,[O\,III]}$ (-1 ± 5)	SW Region
Cluster Stars	Stellar Spectra (25 ± 2)	Sicilia-Aguilar et al. (2005)
Further Central Bubble	$V_{new,[N\,II]}$ (35 ± 3)	Two Regions
…	$V_{new,[O\,III]}$ (27 ± 4)	All three Regions
MIF	[O I] (27 ± 2)	O'Dell & Wen (1992)
…	[O II] (18 ± 1)	Adams (1944); Jones (1992)
…	[N II] (22 ± 2)	All three Regions
…	[S III] (20 ± 4)	Wen & O'Dell (1993)
…	[O III] (17 ± 3)	All three Regions
…	H8+H12 (17 ± 2)	O'Dell et al. (1993)
…	H41α (16 ± 2)	Goicoechea et al. (2015)
…	He^{+} (17 ± 2)	O'Dell et al. (1993)
Backscattered MIF	[N II] (40 ± 2)	All three Regions
…	[S III] (36 ± 4)	Wen & O'Dell (1993)
…	[O III] (39 ± 1)	All three Regions

Notes.
[a] Ca II 393.4 nm.
[b] Na I 589.6 nm.

ORCID iDs

C. R. O'Dell https://orcid.org/0000-0003-3323-2310

References

Abel, N. P., Brogan, C. L., Ferland, G. J., et al. 2004, ApJ, 609, 247
Abel, N. P., Ferland, G. J., & O'Dell, C. R. 2019, ApJ, 881, 130
Abel, N. P., Ferland, G. J., O'Dell, C. R., Shaw, G., & Troland, T. H. 2006, ApJ, 644, 344
Abel, N. P., Ferland, G. J., O'Dell, C. R., & Troland, T. H. 2016, ApJ, 819, 136
Adams, W. S. 1944, PASP, 56, 119
Arthur, S. J. 2012, MNRAS, 421, 1283
Baldwin, J. A., Ferland, G. J., Martin, P. G., et al. 1991, ApJ, 374, 580
Balick, B., Gammon, R. H., & Hjellming, R. M. 1974, PASP, 86, 616
Berné, O., Marcelino, N., & Cernicharo, J. 2014, ApJ, 795, 13
Castañeda, H. O. 1988, ApJS, 67, 93
Chuss, D. T., Andersson, B. –G., Bally, J., et al. 2019, ApJ, 872, 187
Crutcher, R. M. 1999, ApJ, 520, 706
Doi, T., O'Dell, C. R., & Hartigan, P. 2004, AJ, 127, 3456
Ferland, G. J. 2001, PASP, 113, 41
Gagné, M., Oksala, M. E., Cohen, D. H., et al. 2005, ApJ, 628, 986

García-Díaz, Ma. T., & Henney, W. J. 2007, AJ, 133, 952
García-Díaz, Ma.-T., Henney, W. J., López, J. A., & Doi, T. 2008, RMxAA, 44, 181
Goicoechea, J. R., Teyssier, D., Etxaluze, M., et al. 2015, ApJ, 812, 75
Gómez, L., Rodríguez, L. F., Loinard, L., et al. 2005, ApJ, 635, 1166
Greenstein, J. L., & Henyey, L. G. 1939a, ApJ, 89, 647
Greenstein, J. L., & Henyey, L. G. 1939b, ApJ, 89, 653
Großschedl, J. E., Alves, J., Texiera, P. S., et al. 2019, A&A, 622, 149
Güdel, M., Briggs, K. R., Montmerle, T., et al. 2008, Sci, 319, 309
Hartigan, P., Raymond, J., & Hartmann, L. 1987, ApJ, 316, 323
Henney, W. J. 1998, ApJ, 503, 760
Howarth, I. D., & Prinja, R. K. 1989, ApJS, 69, 527
Jones, M. R. 1992, PhD thesis, Rice Univ.
Kong, S., Arce, H. G., Feddersen, J. R., et al. 2018, ApJS, 236, 25
Kounkel, M., Hartmann, L., Loinard, L., et al. 2016, ApJ, 834, 142
Morris, P. W., Gupta, H., Nagy, Z., et al. 2016, ApJ, 829, 15
Muench, A., Getman, K., Hillenbrand, L., & Preibisch, T. 2008, in Handbook of Star-forming Regions, Vol. 1: The Northern Sky, ed. B. Reipurth (San Francisco, CA: ASP), 483
O'Dell, C. R. 2001, ARA&A, 39, 9
O'Dell, C. R. 2018, MNRAS, 478, 1017
O'Dell, C. R., & Harris, J. A. 2010, AJ, 140, 985
O'Dell, C. R., Henney, W. J., Abel, N. P., et al. 2009, AJ, 137, 367
O'Dell, C. R., Kollatschny, W., & Ferland, G. J. 2017, ApJ, 837, 151
O'Dell, C. R., Muench, A., Smith, N., & Zapata, L. 2008, in Handbook of Star-forming Regions, Vol. 1: The Northern Sky, ed. B. Reipurth (San Francisco, CA: ASP), 544
O'Dell, C. R., Valk, J. H., Wen, Z., & Meyer, D. M. 1993, ApJ, 403, 478
O'Dell, C. R., & Wen, Z. 1992, ApJ, 387, 229
O'Dell, C. R., & Wong, S. K. 1996, AJ, 111, 846
O'Dell, C. R., & Yusef-Zadeh, F. 2000, ApJ, 120, 382
Pabst, C., Higgins, R., Goicoechea, J. R., et al. 2019, Natur, 565, 618
Pankonin, V., Walmsley, C. M., & Harwit, M. 1979, A&A, 75, 34
Rodríguez, L. F., Poveda, A., Lizano, S., & Allen, C. 2005, ApJ, 627, L65
Sicilia-Aguilar, A., Hartmann, L. W., Szentgyorgyi, A. H., et al. 2005, AJ, 129, 363
Troland, T. H., Goss, W. M., Brogan, C. L., Crutcher, R. M., & Roberts, D. A. 2016, ApJ, 825, 2
van der Werf, P. P., & Goss, W. M. 1989, A&A, 224, 209
van der Werf, P. P., & Goss, W. M. 1990, A&A, 364, 157
van der Werf, P. P., Goss, W. M., & O'Dell, C. R. 2013, ApJ, 762, 101
Wen, Z., & O'Dell, C. R. 1993, ApJ, 409, 262
Wen, Z., & O'Dell, C. R. 1995, ApJ, 438, 784
Zuckerman, B. 1973, ApJ, 183, 163